APSB
Acta Pharmaceutica Sinica B
2021
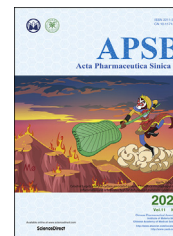
ORIGINAL ARTICLE

Boosting 5-ALA-based photodynamic therapy by a liposomal nanomedicine through intracellular iron ion regulation

Airong Li[†], Chenglin Liang[†], Lihua Xu, Yiyang Wang, Wei Liu, Kaixiang Zhang[*], Junjie Liu[*], Jinjin Shi[*]

Henan Key Laboratory of Targeting Therapy and Diagnosis for Critical Diseases, School of Pharmaceutical Sciences, Zhengzhou University, Zhengzhou 450001, China

Abstract   5-Aminolevulinic acid (5-ALA) has been approved for clinical photodynamic therapy (PDT) due to its negligible photosensitive toxicity. However, the curative effect of 5-ALA is restricted by intracellular biotransformation inactivation of 5-ALA and potential DNA repair of tumor cells. Inspired by the crucial function of iron ions in 5-ALA transformation and DNA repair, a liposomal nanomedicine (MFLs@5-ALA/DFO) with intracellular iron ion regulation property was developed for boosting the PDT of 5-ALA, which was prepared by co-encapsulating 5-ALA and DFO (deferoxamine, a special iron chelator) into the membrane fusion liposomes (MFLs). MFLs@5-ALA/DFO showed an improved pharmaceutical behavior and rapidly fused with tumor cell membrane for 5-ALA and DFO co-delivery. MFLs@5-ALA/DFO could efficiently reduce iron ion, thus blocking the biotransformation of photosensitive protoporphyrin IX (PpIX) to heme, realizing significant accumulation of photosensitivity. Meanwhile, the activity of DNA repair enzyme was also inhibited with the reduction of iron ion, resulting in the aggravated DNA damage in tumor cells. Our findings showed MFLs@5-ALA/DFO had potential to be applied for enhanced PDT of 5-ALA.

---

*Corresponding authors. Tel./fax: +86 371 67781908.
E-mail addresses: zhangkx@zzu.edu.cn (Kaixiang Zhang), liujunjie@zzu.edu.cn (Junjie Liu), shijinyxy@zzu.edu.cn (Jinjin Shi).
[†]These authors made equal contributions to this work.

1. Introduction

Photodynamic therapy (PDT), as a minimally invasive therapeutic method, has been widely used in tumor therapy due to the unique advantages of simplicity, high efficiency, and negligible drug resistance[1,2]. PDT relies on photosensitizers (PS) to convert light energy into chemical energy, which reacts with oxygen to generate reactive oxygen species (ROS)[3–5]. Recently, many PSs have been developed and explored in the laboratory, such as porphyrin derivatives, 5-ALA, and chlorine e6 (Ce6)[6,7]. Among them, 5-ALA is an endogenous non-protein amino acid and a precursor to PpIX[8–10]. Once being uptake by cells, it is converted into photosensitive PpIX after a series of reactions, and plays the function of PDT after light irradiation[11–13]. The intracellular biotransformation of 5-ALA endows the ultralow phototoxicity. For this reason, 5-ALA is widely used in cancer treatment and it was approved for glioma surgery by the US Food and Drug Administration (FDA) in 2017[14–16].

Unfortunately, after the conversion of 5-ALA to photosensitive PpIX, the rapid binding of PpIX with iron ions further converted to heme without photosensitive activity, resulting in the loss of intracellular PS, thus significant limiting the efficiency of PDT[17–19]. Previous studies have shown that the reduction of intracellular iron ions can significantly block the biotransformation of PpIX to HEME[8,20,21]. Therefore, the decrease of intracellular iron can enhance the accumulation of PpIX, further leading to the increase of ROS in tumor cells[22]. ROS usually causes the oxidative damage to DNA, proteins and phospholipids, and ROS-mediated DNA damage can significantly induce

apoptosis of tumor cells. However, high expressed DNA repair enzymes in tumor cells would rapidly excise injury DNA and restore the genome sequence by homologous recombination[23]. Therefore, reducing the activity of DNA repair enzymes would be beneficial to PDT in tumor cells. Interestingly, the DNA repair enzyme (such as ALKBH2/3) is a ferrous ion (Fe^{2+})-dependent enzyme, and the decrease of intracellular free Fe^{2+} would significantly inhibit its activity[24,25]. Hence, if we can regulate the intracellular Fe^{2+}, it would be an efficient strategy for increasing the accumulation of PpIX and aggravating the ROS-mediated DNA injury in tumor cells, which can significantly improve the PDT efficiency of 5-ALA.

Membrane fusion was defined as the joining of two closely opposed lipid bilayers to form a single bilayer with minimal leakage of content 26. The composition of natural membrane is complex and different lipids may have different roles in membrane function. For example, 1,2-dioleoyl-sn-glycero-3-phosphocholine (DOPC), dioleoyl phosphatidylethanolamine (DOPE), sphingomyelin (SM), cholesterol (CH) are the main lipid species in mammalian membrane[27]. Thus, MFLs composed of DOPC, DOPE, SM and CH were proved to be the most sui– structures for membrane fusion[26]. Studies have shown that MFLs could be internalized into tumor cells through membrane fusion, and drugs encapsulated in liposomes can enter the cytoplasm directly. This property increases the uptake rate of the drug by tumor cells[28]. Herein, we report a liposomal nanomedicine for boosting the PDT of 5-ALA though intracellular iron ion regulation (Scheme 1). Specifically, we used DOPC/DOPE/CH/SM as the building units to prepare MFLs, which acted as a nanocarrier
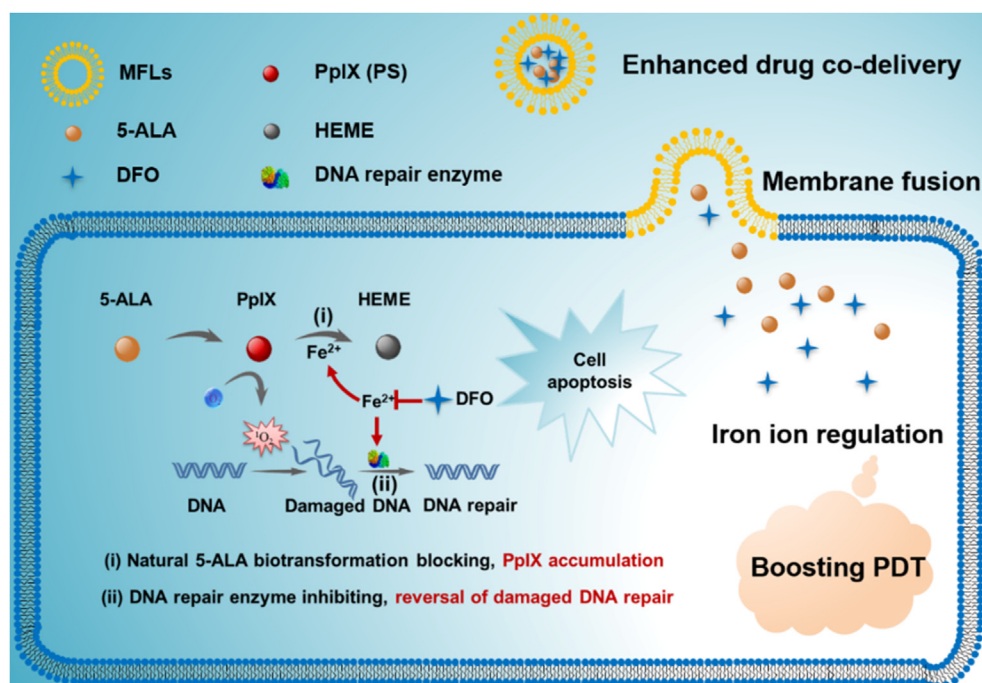
Scheme 1 Schematic diagram of the liposomal nanomedicine (MFLs@5-ALA/DFO) for boosting the PDT of 5-ALA through intracellular iron ion regulation.

for 5-ALA and deferoxamine (DFO). MFLs significantly improved the *in vivo* pharmaceutical behavior and achieved the co-delivery of 5-ALA and DFO to tumor cells. Importantly, the drug-loaded MFLs rapidly fused with the tumor cell membrane and released 5-ALA and DFO into the cytoplasm directly. DFO served as an intracellular regulator of iron ion, thus blocking the biotransformation of PpIX to HEME, realizing a significant increase of intracellular accumulation of PpIX[21,29]. Meanwhile, the activity of DNA repair enzyme was inhibited with the decrease of the intracellular iron ion, resulting in aggravating the ROS-mediated DNA injury in tumor cells. Such a liposomal nano-medicine that integrating the interference of natural 5-ALA biotransformation and the reversal of damaged DNA repair through iron ion regulation would significantly enhance the PDT efficiency of 5-ALA.

2. Materials and methods

2.1. Materials

5-Aminolevulinic acid hydrochloride (5-ALA, purity ≥98%), DFO, Sphingomyelin (SM), α-ketoglutarate were bought from Sigma−Aldrich (St. Louis, MO, USA). 1,2-Dioleoyl-*sn*-glycero-3-phosphocholine (DOPC), dioleoyl phosphatideylethan-olamine (DOPE), dipalmitoyl-*sn*-glycero-3-phosphocholine (DPPC), cholesterol (CH) were bought from Switzerland Solarbio Co., Ltd. (Beijing, China). DpnII was bought from BioLabs Inc. (Beijing, China). FerroOrange was purchased from Goryo Chemical Inc. (Hokkaido, Japan). RPMI 1640 cell culture medium, fetal bovine serum (FBS) were bought from Solarbio Science & Technology Co., Ltd. (Beijing, China). CCK-8, Reactive Oxygen Species Assay Kit (DCFH-DA), DiO, DiI, DAPI, and Annexin V-FITC Apoptosis Detection Kit were obtained from Beyotime Biotechnology (Shanghai, China). Calcein-AM/propidiumiodide (calcein-AM/PI) staining agents were obtained from Yeasen Biotech Co., Ltd. (Shanghai, China). Other reagents were purchased from China National Medicine Corporation Ltd.

2.2. Preparation and characterization

2.2.1. Preparation of MFLs@5-ALA/DFO
Membrane fusion liposomes were prepared by film hydration method[30]. Briefly, the liposome components were mixed with appropriate mass ratio (DOPC/DOPE/SM/CH: 7/6/3/4) in chloroform (3 mL) were evaporated to dryness in a rotary evaporator (RE-52AA, Shanghai, China). The dried mixed lipids were dissolved in 2 mL water containing 5-ALA and DFO, then hydrated and ultrasonically detected using a cell ultrasonic pulverizer (JY 92-II DN, Xinzhi Biological Technology Co., Ltd., Ningbo, China). Next, the prepared nanoparticles were dialyzed in phosphate-buffered saline (PBS, Leagene Biotech Co., Ltd., Beijing, China) for 48 h to remove free 5-ALA and DFO. The resulting MFLs@5-ALA/DFO nano-suspension was stored at 4 °C.

2.2.2. Preparation of CLs@5-ALA/DFO
The preparation of custom liposomes (CLs) is similar to the above steps[31]. Briefly, DPPC (8 mg) and cholesterol (1 mg) were dissolved in chloroform (3 mL). After evaporating to remove the chloroform, the product was dispersed in 5-ALA and DFO solution (2 mL). After incubation at 40 °C for 10 min, the prepared preparation was dialyzed according to the above method. The

solution was dialyzed against PBS for 2 days to remove unencapsulated 5-ALA and DFO. The resulting nano-suspension was stored at 4 °C until use.

2.2.3. Detection of drug entrapment efficiency and loading capacity
Firstly, the standard curves of 5-ALA and DFO were established. For 5-ALA, 0.1 mg/mL of 5-ALA standard solution and acetic acid-sodium acetate buffer solution (pH 5.8) were prepared. Different volumes of 5-ALA were added into ethyl acetoacetate (0.2 mL) and acetic acid-sodium acetate buffer (4 mL). The reaction was carried out at 100 °C for 25 min. Then HCl (4 mL, 4 mol/L) and Fe^{3+} (1 mL, 1 g/L) were added to react for 30 min at 100 °C. The absorbance was detected at 480 nm after cooling to room temperature. For DFO, 1 mmol/L Fe^{3+} with different concentrations DFO was incubated for 5 min at 37 °C. The absorbance was detected at 430 nm by UV−Vis spectrophotometer (UV-2550, Shimadzu, Japan).

The entrapment efficiency (EE, %) of 5ALA and DFO was investigated *via* difference method, and the unencapsulated drugs were detected *via* UV−Vis assay (for 5-ALA, 480 nm; DFO, 430 nm) according to the standard curves (Supporting Information Fig. S2). The loading capacity (LC, %) and entrapment efficiency (EE%) of the prepared formulations were determined using the following Eqs. (1) and (2):

$$\text{Entrapment efficiency}(\%) = \frac{(\text{Amount of the drug}-\text{Amount of free the drug})}{\text{Amount of the drug}} \times 100 \quad (1)$$

$$\text{Loading capacity}(\%) = \frac{\text{Amount of drug in the formulation}}{\text{Amount of nanoparticles}} \times 100 \quad (2)$$

2.2.4. Release profiles of 5-ALA and DFO from MFLs
5-ALA and DFO release from MFLs were measured using dialysis membranes (MW cut of 10−12 kDa) in phosphate-buffered saline (PBS) at 37 °C for 36 h, and the dialysis samples were collected periodically and quantified the 5-ALA and DFO according to the method in 2.2.3.

2.2.5. To test the complexation ability of DFO to Fe^{2+} and Fe^{3+}
DFO: Fe^{2+} and DFO: Fe^{3+} solutions with different volume ratios (1:0.5, 1:1, 1:2) were prepared, mixed and incubated at 37 °C for 5 min. The complexation ability of different incubation time at 37 °C was investigated when the volume ratio was 1:1. The absorbance was detected at 430 nm by UV−Vis spectrophotometer.

2.2.6. The investigation of the diffusion ability of iron ions through MFLs
The amount of 0.1 mmol/L of Fe^{2+} was taken and co-incubated with 1 mL of MFLs and MFLs@DFO at 37 °C for 12 h, respectively. After centrifugation, the supernatant was taken and 1,10-phenanthroline was added to detect the content of Fe^{2+} *via* UV−Vis spectrophotometer (510 nm). In addition, 200 μL of MFLs and MFLs@DFO precipitation were taken out and 800 μL of acetonitrile was added to demulsify, respectively. Finally, the supernatant was collected by centrifugation and the iron ion content was measured using Eq. (3)

Iron ion content (%)

$$= \text{The content of iron ions in the sample} \quad (3)$$
$$/\text{The total content of iron ions} \times 100$$

2.2.7. Detection of ALKBH2 enzyme activity

The activity of ALKBH2 (Abcam, ab105622, USA) was detected according to the previous steps[24,32]. The oligonucleotide substrate is 5′-ATTGCCATTCTCGATAGG (m1A) TCCGGTCAAACC-TAGACGAA-3′ (Sangon Biotech, Shanghai, China). The complementary oligo-nucleotide is 5′-TTCGTCTAGGTTTGACCGG ATCCTATCGAGAATGGCAAT-3′[24] (Sangon Biotech, Shanghai, China). The oligonucleotide substrate and the complementary substrate were mixed and heated to 90 °C for 1 min. Then, the substrates were cooled at 1 °C/min until 4 °C. After synthesis of double chain, DNA repair reactions were operated with the 1 μmol/L oligonucleotide substrates and 1 μmol/L recombinant ALKBH2 proteins in the reaction buffer (40 mmol/L α-ketoglutarate, 50 mmol/L Tris-HCl, 0.28 mmol/L $FeSO_4$, 10 mmol/L $MgCl_2$, 2 mmol/L L-ascorbic acid and 15 mmol/L DFO) for 2 h at 37 °C. Then the reactions were digested with DpnII restriction enzyme for 3 h at 37 °C. The repaired dsDNA was detected by 12% nondenatured TBE-PAGE gel.

2.3. Cell culture

The mice melanoma B16−F10 cell line in this study was from the China Center for Type Culture Collection at Wuhan University (Hubei, China). The B16−F10 cells were cultured in RPMI 1640 medium with 10% FBS. All cells were maintained at 37 °C, 5% CO_2 in all experiments.

2.3.1. Membrane fusogenic property of MFLs and CLs

The B16−F10 cells were seeded and cultured in confocal dish (2×10^5 cells per dish) for 24 h, then treated with DiO-labeled MFLs and CLs for 4 h. After, the cell membrane was stained with DiI for 15 min, and the remaining DiI was washed with PBS for three times. Then the cells were fixed with 4% paraformaldehyde for 10 min and washed with PBS for three times. The cell nucleus were stained by DAPI (10 μg/mL) solution. Ten minutes later, residual DAPI was removed and washed, and then the samples were imaged directly by a confocal laser-scanning microscopy (CLSM, Leica TCS SP8, Germany).

2.3.2. Cellar internalization of MFLs@5-ALA/DFO

The B16−F10 cells were seeded into confocal dish (2×10^5 cells per dish) for 24 h of incubation and then incubated with control, 5-ALA, DFO, 5-ALA + DFO, CLs@5-ALA/DFO, MFLs@5-ALA/DFO (with the same dose of 5-ALA and DFO: 1 mmol/L and 100 μmol/L respectively) for 4 h. Other treatments were the same as the above steps.

2.3.3. The detection of iron ion in cell

The B16−F10 cells were seeded into confocal dish (2×10^5 cells per dish) for 24 h of incubation and then treated with control, 5-ALA, DFO, 5-ALA + DFO, CLs@5-ALA/DFO, MFLs@5-ALA/DFO (with the same dose of 5-ALA and DFO: 1 mmol/L and 100 μmol/L respectively) for 4 h. After that, FerroOrange working solution (1 mL, 1 μmol/L) was added to each dish and incubated for a certain period of time, and then the samples were observed directly by a confocal laser-scanning microscopy (CLSM, Leica TCS SP8).

2.3.4. ROS generation of MFLs@5-ALA/DFO in B16−F10 cells

DCFH-DA (a ROS detection kit) was used to evaluate ROS production in cell level[33]. First, B16−F10 cells were seeded in a 6-well plate (2×10^5 cells per well) and cultured for 24 h then the medium was removed and washed with PBS. Then, the cells were incubated with control, 5-ALA, DFO, 5-ALA + DFO, CLs@5-ALA/DFO, MFLs@5-ALA/DFO (with the same dose of 5-ALA and DFO: 1 mmol/L and 100 μmol/L respectively) for 4 h and then replaced by fresh medium. The cells were irradiated with 532 nm laser (300 mW/cm^2) (Xi'an Lei Ze Electronic Technology Co., Ltd., Xi'an, China) for 5 min, and an addition 1 μL of DCFH-DA for 30 min. The ROS generation of all samples were observed using a Fluorescence Microscope (Zeiss, LSM 510, Shanghai, China).

2.3.5. Cytotoxicity assay

The cytotoxicity assay of 5-ALA, 5-ALA + DFO, MFLs@5-ALA/DFO was conducted with CCK-8 assay kit[34]. Briefly, B16−F10 cells were seeded in 96-well plates at 8×10^3 per well and cultured in 200 μL of fresh complete medium for 12 h. After that, the cells were incubated in medium containing 5-ALA, 5-ALA + DFO, MFLs@5-ALA/DFO with different concentrations for 4 h, and then replaced by fresh medium. Each hole was irradiated with 532 nm laser (300 mW/cm^2) for 5 min. After incubating for 24 h, 10 μL of CCK-8 was added into the medium for 3 h. The optical density (OD) was measured at 450 nm by a microplate reader (Synergy H1, USA). Cell viability of different nanoparticles were calculated by the following Eq. (4):

$$\text{Cell viability}(\%) = \left(OD_{\text{sample}} - OD_{\text{blank}}\right)/\left(OD_{\text{control}} - OD_{\text{blank}}\right) \times 100 \quad (4)$$

2.3.6. Live/dead cell staining by calcein-AM and propidium Iodide (calcein-AM/PI)

B16−F10 cells were seeded in 96-well plates at 8×10^3 per well and cultured in 200 μL of fresh complete medium for 12 h. After that, the cells were incubated with control, 5-ALA, DFO, 5-ALA + DFO, MFLs@5-ALA/DFO (with the same dose of 5-ALA and DFO: 1 and 100 μmol/L respectively, 200 μL) for 4 h. After that, the cells were irradiated with 532 nm laser (300 mW/cm^2, 5 min) and incubated with culture medium for another 24 h. Subsequently, the cells were stained with calcein-AM/PI and then monitored using a fluorescence microscope (Zeiss).

2.3.7. Apoptosis analysis

The apoptosis of B16−F10 cells was detected by Annexin V/Propidium Iodide Apoptosis Detection Kit. The cells received different treatments according to the above procedure. After treatments, the cells were digested with trypsin without EDTA and collected, washed with PBS at three times and re-suspended in 500 μL Annexin V binding buffer. Further, 5 μL Annexin V-FITC and PI were added. After mixing, the reaction was carried out at room temperature without light for 15 min, and analyzed by flow cytometry (FACS Aria III, BD, USA).

2.3.8. The detection of DNA damage by Western blotting

The standard operation of Western blotting was performed according to previous research[35]. The cells received different treatments according to the above procedure. After treatments, B16−F10 cells were cleaved in RIPA lysate containing protease inhibitor for 40 min. The samples were centrifuged and the supernatant was collected. Then, the sample buffer was added and denatured at 100 °C. The samples were separated by 12% SDS-

PAGE and transferred into PVDF membranes. Blocked with 5% BSA for 1 h, incubated with the γH2AX (Abcam, ab81299, UK) and GAPDH (Abcam, ab8245, UK) at 4 °C overnight, washed three times with 1 × TBST, then membranes were incubated with the secondary antibodies at room temperature for 2 h. After washed for three times, ECL hypersensitive liquid (Beyotime Biotechnology, Shanghai, China) was using for detecting.

2.3.9. Comet assay

The comet assay was performed as described previously[36]. The cells received different treatments according to the above procedure. After treatments, the B16−F10 cells were trypsinized, collected and kept on ice until use. Briefly, 100 μL of 0.5% normal melting point agarose (NMPA) was dropped on slides and covered by 24 mm × 50 mm coverslips and solidified at 4 °C for 10 min. Then 30 μL of cell suspension was mixed with 50 μL of 0.5% low melting point agarose (LMPA), and then spread on the slides, covered with the cover slides, and solidified at 4 °C for 10 min. After the agarose had solidified, then the coverslips were removed, and another 90 μL of LMPA was added, and coverslips were placed on top. The coverslips were removed again, and the slides were placed in cell lysate solution (2.5 mol/L NaCl, 100 mmol/L EDTA, 10 mmol/L Tris, 1% Triton X-100, pH 10) to lysate at 4 °C for 2 h. The slides were then placed in water and rinsed. The slides were put into the alkaline electrophoresis solution (1 mmol/L EDTA-2Na, 300 mmol/L NaOH, pH 13) and kept away from light for 20 min. Electrophoresis was performed in electrophoresis solution for 25 min at 25 V and 300 mA. Then the slides were washed in neutralizing buffer (0.4 mol/L Tris-HCl, pH 7.5) for three times/5 min. Finally, PI staining solution (25 μg/mL) was dropped on the slides, placed for 15 min and washed. The DNA trail in the cells of each group was observed under the fluorescence microscope (Zeiss), and the pictures were recorded.

2.4. Animal experiments

All animal experiments were performed according to the guidelines approved by Henan Laboratory Animal Center. B16−F10 cells (2×10^6 cells/mL) were injected subcutaneously into female C57 mice (Henan Province Experimental Animal Center, Zhengzhou, China) to establish tumor bearing mice model. When the tumor volume reached 60−100 mm^3, they were used for the next step of the experiment. The tumor volume calculated by the following Eq. (5):

$$\text{Tumor volume} = (\text{Tumor width})^2 \times (\text{Tumor length})/2 \qquad (5)$$

2.4.1. Biodistribution of CLs and MFLs in vivo

IR780 (a near infrared fluorescent dye, Sigma−Aldrich) was used to label the CLs and MFLs. Tumor-bearing mice were injected with free IR780, CLs@IR780 and MFLs@IR780 (with the same concentration of IR780, 100 μg/mL, 200 μL), respectively. The distribution of free IR780, CLs@IR780 and MFLs@IR780 in tumor-bearing mice was observed at the indicated time points of 1, 2, 4, 6, 8, 12, 24 and 36 h by a small animal imaging system (Kodak, USA). After that, the mice were sacrificed by dislocation and the heart, liver, spleen, lung, kidney and tumor were taken for ex vivo observation.

2.4.2. Evaluation of antitumor effect in vivo

Tumor-bearing mice were randomly divided into 7 groups (6 mice per group). The tumor-bearing mice were treated by tail vein every other day with (1) saline, (2) 5-ALA, (3) DFO, (4) 5-ALA + DFO, (5) MFLs@5-ALA, (6) CLs@5-ALA/DFO, (7) MFLs@5-ALA/DFO (at the dose of 25 mg/kg of 5-ALA) 6 h after injection, the mice were irradiated with 532 nm laser (300 mW/cm^2) for 5 min. Meanwhile, the tumor volume and body weight of mice were recorded during treatment. After 14 days of treatment, the mice were sacrificed and the main organs including tumor tissues were collected. The main organs were stained with hematoxylin and eosin (H&E) to evaluate the side effects of MFLs@5-ALA/DFO, and the tumor tissues were stained with H&E and terminal deoxynucleotidyl trans-ferase dUTP nick end labeling (TUNEL) to evaluate the anti-tumor effect. In addition, the tumor tissues were stained with FerroOrange and DHE to detect the level of Fe^{2+} and the production of ROS, respectively.

2.5. Statistical analysis

Experimental data was shown as mean ± SD. All statistical analyses were processed with Graph Pad Prism 6.0 (La Jolla, CA, USA). The data were analyzed to determine the difference between groups, by one-way or two-way ANOVA test. A value of *$P < 0.05$ was considered statistically significant.

3. Results and discussion

3.1. The characterization of MFLs@5-ALA/DFO

MFLs@5-ALA/DFO were prepared with DOPC/DOPE/CH/SM as the building units to prepare MFLs, which acted as a nanocarrier for 5-ALA and DFO. The morphology of blank MFLs was investigated by transmission electron microscopy (TEM, FEI, USA). According to the results of Fig. 1A and Supporting Information Fig. S1, the prepared MFLs showed a uniform spherical structure with the diameter of ∼70 nm. After 5-ALA and DFO loading, the morphology of MFLs@5-ALA/DFO showed no significant difference, the possible reason is that the loaded drugs with high water solubility were wrapped in the hydrophilic layer of MFLs (Fig. 1B). The particle size and zeta potential of MFLs@5-ALA/DFO were detected via dynamic light scattering (DLS, Zetasizer Nano ZS-90, Malvern, UK), showing hydrated particle size of MFLs@5-ALA/ DFO was 90 ± 10 nm (Fig. 1C), and the zeta potential (ζ) of MFLs and MFLs@5-ALA/DFO was about −15.4 ± 2.3 and −16.1 ± 1.8 mV, respectively (Fig. 1D). In addition, MFLs@5-ALA/DFO had a good stability in water, and showed no significant change in the particle size and zeta potential within 14 days of monitor (Fig. 1E). The encapsulation efficiency (EE%) of 5-ALA and DFO in MFLs@5-ALA/DFO was ∼ 43% and ∼ 55% when the drug lipid ratio of 5-ALA and MFLs was 1:2. When the ratio of drug to lipid increased, the entrapment efficiency did not change much. The drug loading capacity (LC, %) of 5-ALA and DFO were 16.9% and 2.1%, respectively. More importantly, the PDI of MFLs@5-ALA/DFO was relatively low (Fig. 1F), therefore, the drug to lipid of 1:2 was chosen for the following experiments. Next, we investigated the release rates of 5-ALA and DFO in vitro. According to the result shown in Supporting Information Fig. S3, we can see that for 5-ALA, the release reaches a peak (about 13%) at the sixth hour, and then drops slightly and remains stable. Similarly, the DFO peaks at the 10 h (about 10%) and then balances. It can be seen
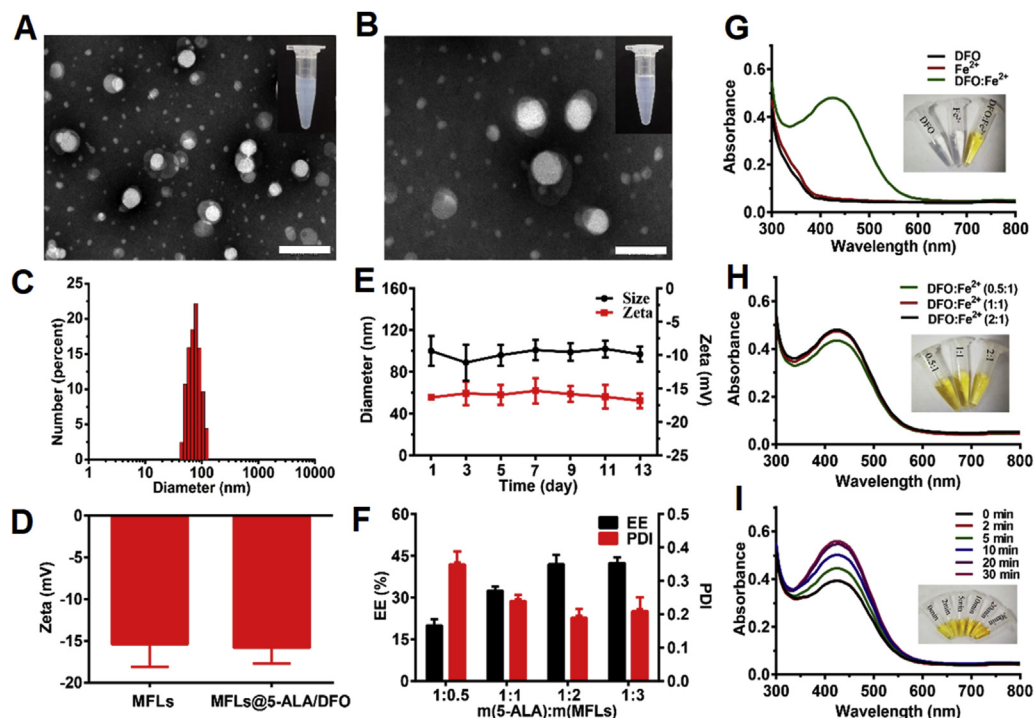
Figure 1 Synthesis and characterization of MFLs@5-ALA/DFO. Transmission electron microscopy images of MFLs (A) (scale bar = 200 nm) and MFLs@5-ALA/DFO (B) (scale bar = 100 nm), and the appearance picture (the inset). (C, D) Size and zeta potential of the MFLs analyzed by DLS, respectively. (E) The stability of MFLs@5-ALA/DFO (F) The encapsulation efficiency (EE, %) and polymer dispersity index (PDI) of MFLs@5-ALA/DFO. (G, H, I) The UV−Vis spectra of DFO complex Fe^{2+} at 430 nm and picture of complexing appearance (the inset). Data are presented as means $\pm$ SD ($n = 3$).

from this that MFLs containing 5-ALA and DFO are less released *in vitro*, which is conducive to maintaining the stability of the drug in the blood circulation and efficiently delivering the drug into the tumor cells.

In this study, DFO served as an intracellular regulator of iron ion, thus enhancing the PDT efficiency of 5-ALA. DFO was encapsulated in MFLs, and once the iron ion in blood circulation or tumor stroma diffuses through MFLs, it would saturate the loaded DFO. To investigate whether iron ion could diffuse through MFLs, MFLs and MFLs@DFO (with the same concentration of MFLs) were incubated with 0.1 mmol/L of iron ion for 12 h, respectively, and then the iron ion in centrifugal supernatant or in MFLs, MFLs@DFO was detected (Supporting Information Fig. S4). According to the above results, compared with no treatment group (without MFLs or MFLs@DFO), no significant difference of iron ion in centrifugal supernatant in the case of MFLs or MFLs@DFO. More importantly, there is no significant difference of iron ion in MFLs and MFLs@DFO, showing that after 12 h of incubation, iron ion could not diffuse through MFLs. Thus, DFO in MFLs could display the iron removal effect until it was released in the tumor cells.

In addition, the complexation ability of DFO to Fe^{2+} was measured by UV spectrophotometer, and the result was shown in Fig. 1G. DFO and Fe^{2+} were colorless liquids and had no characteristic absorption, while the color showed an obvious change with the appearance of an obvious characteristic absorption peak at 430 nm, indicating that Fe^{2+} could be complexed by DFO.

Furthermore, the complexation efficiency reached the maximum when the ratio of DFO to Fe^{2+} is 1:1 (Fig. 1H), the complexation rate increased with the prolongation of time and reached a stable level at about 20 min (Fig. 1I). Furthermore, the complexation ability of DFO to Fe^{3+} was also investigated (Supporting Information Fig. S5).

3.2. Intracellular iron ion regulating mediated PpIX accumulation and DNA repair enzyme inhibition

In this study, a liposomal nanomedicine was prepared for boosting the PDT of 5-ALA though intracellular iron ion regulation. The efficient cellular uptake and rapid release of the loaded drugs in tumor cells are the key to its function. Therefore, as part of rational design, an MFLs was used as the drug carrier for efficient intracellular delivery. To verify the membrane fusion property of the prepared MFLs, a custom liposome (non-membrane fusion) was used as a control. In brief, CLs and MFLs were labeled with DiO (membrane dye, green fluorescence) and the membrane of B16−F10 cells was labeled with DiI (membrane dye, red fluorescence). The tumor cells were incubated with CLs and MFLs for 4 h, and the distribution of fluorescence were shown in Fig. 2A and Supporting Information Fig. S6. As predicted, the green fluorescence of DiO was observed mainly in the cytoplasm and less in the cell membrane in the case of CLs-treated group. Nevertheless, the green fluorescence of DiO in the case of MFLs group mainly distributed in the cell membrane, and had a high co-
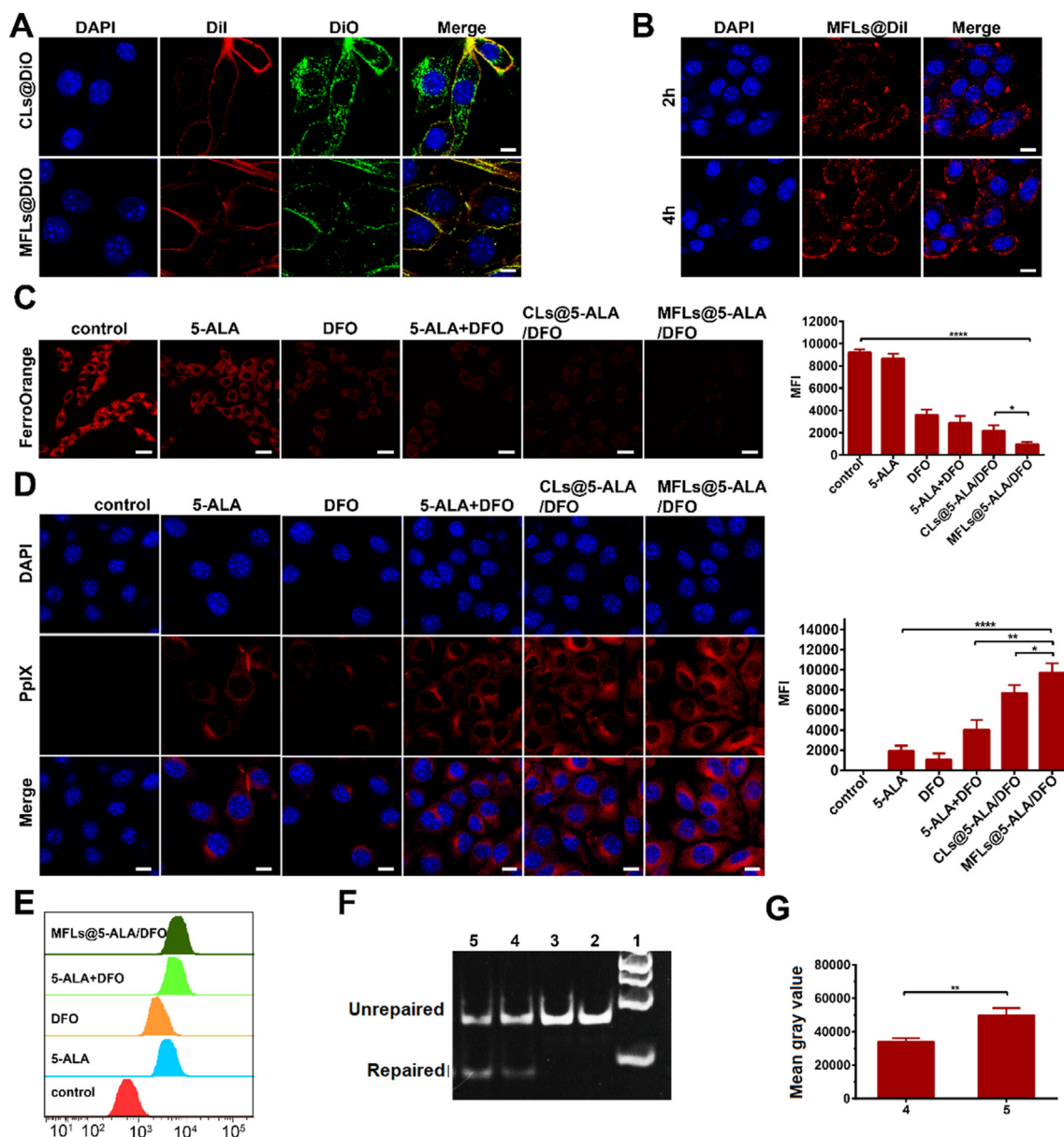
Figure 2 Intracellular iron ion regulating mediated PpIX accumulation and DNA repair enzyme inhibition. (A) The membrance fusion of CLs@DiO and MFLs@DiO (scale bar = 10 μm), the distribution of MFLs@DiI in B16−F10 cells (B) (scale bar = 10 μm). (C) The detection of Fe^{2+} after incubating with B16−F10 cells for 4 h (scale bar = 25 μm). (D, E) The transformation of 5-ALA analyzed after incubating with B16−F10 cells for 4 h by CLSM (scale bar = 10 μm) and flow cytometry, respectively. (F) DFO inhibits ALKBH2 repair of m1A in dsDNA by using the DpnII digestion assay and semi-quantitative analysis (G), 1: maker, 2: dsDNA (m1A), 3: dsDNA (m1A)+DpnII, 4: dsDNA (m1A)+ ALKBH2+Fe^{2+}+DFO + DpnII, 5: dsDNA (m1A)+ALKBH2+Fe^{2+}+DpnII. Data are presented as means ± SD (n = 3). ****$P < 0.0001$, **$P < 0.01$, *$P < 0.05$.

location rate with DiI, indicating the membrane fusion property of MFLs. In addition, the speed of the membrane fusion between MFLs and B16−F10 cells was also investigated, and the results showed that MFLs could fuse with the cell membrane within 2 h (Fig. 2B), indicating the rapid fusion between MFLs and B16−F10 cells. Moreover, in order to verify whether the high co-localization rate of DiO and DiI is owing to the unsteady DiO and DiI label in MFLs and cytomembrane of B16−F10 cells. The DiO release from MFLs and the fluorescence change of DiO labeled MFLs were detected and the fluorescence change of DiI labeled B16−F10 tumor cells were detected *via* CLSM. As the results

show (Supporting Information Figs. S7 and S8), no significant fluorescence change of DiO labeled MFLs was observed after 12 h of incubation, and only ∼3.2% of DiO was released after 12 h of incubation, suggesting that DiO labeled MFLs was stable for at least 12 h. In addition, B16−F10 cells labeled with DiI showed no significant decrease of fluorescence, indicating that DiI labeled B16−F10 cells was stable for at least 12 h.

Once the liposomal nanomedicine was fused with the cell membrane, the loaded drugs (5-ALA and DFO) would be released into cytoplasm, and the intracellular iron ion would show a significant decrease. To clarify this, a free iron probe (FerroOrange)

was utilize for monitoring the iron ion in B16−F10 cells after receiving different treatments. As can be seen from the results, compared with the control group, DFO-treated cells showed a significant decrease in iron ion (Fig. 2C), indicating that DFO could effectively complex the iron ion in tumor cells. Furthermore, MFLs@5-ALA/DFO-treated cells showed the strongest decrease in iron ion, demonstrating that MFLs could bring more DFO into the tumor cells than that of other treatments (including CLs@5-ALA/DFO). The significant reduction of the intracellular iron results in the blockade of PpIX biotransformation, realizing a significant increase of intracellular accumulation of PpIX. Therefore, the levels of PpIX in B16−F10 cells after different treatments were observed *via* the spontaneous red fluorescence of PpIX, and the results are shown in Fig. 2D. More importantly, compared with the 5-ALA group, a large amount of red fluorescence was observed in tumor cells when incubated with 5-ALA + DFO (Fig. 2D), suggesting the blockade of the biotransformation induced the significant accumulation of PpIX. As predicted, in the case of MFLs@5-ALA/DFO group, more red fluorescence was observed than that of other groups including CLs@5-ALA/DFO group (Fig. 2D), further demonstrating the improved drug delivery ability of MFLs. Interestingly, PpIX accumulation was also observed in the case of DFO group, and there was no significant difference between DFO and 5-ALA. In mammalian cells, the intracellular biosynthesis of 5-ALA and the biotransformation of 5-ALA is a natural and inherent mechanism. DFO could obviously decrease the intracellular iron ion, which was proved by Fig. 2C, and then suppressed the biotransformation of PpIX to HEME, further leading to the endogenous PpIX accumulation in B16−F10 cells. For 5-ALA-treated cells, the biosynthetic PpIX could be converted to hemedue to the high intracellular concentration of iron ion. It was reported that melanoma cell cells exhibit a trend toward enhanced iron acquisition and retention, and the content of endogenous iron ions in melanoma cells is significantly higher than that in other cells[37,38], which may be one of the potential reasons for this phenomenon. The endogenous PpIX accumulation in DFO group and the biotransformation of PpIX to hemein 5-ALA group leads to almost the same amount of PpIX in B16−F10 cells. Furthermore, compared with DFO or 5-ALA-treated cells, the amount of PpIX in 5-ALA + DFO-treated cells showed significantly increase, suggesting the blockade of the biotransformation induced the significant accumulation of PpIX, which could bring more benefit for 5-ALA-based PDT. The results are also confirmed by the results of flow cytometry (Fig. 2E).

Next, the inhibitory effect of DFO on ALKBH2 was evaluated by enzyme digestion assay. ALKBH2 enzyme needs Fe^{2+} as a necessary cofactor to repair DNA damage, while DpnII is more sensitive to the damaged oligonucleotide chain. When the damaged DNA strand was repaired, the restriction enzyme DpnII could specific shear the repaired DNA strand. Results as shown in Fig. 2F, Supporting Information Figs. S9 and S10, the damaged dsDNA was not cut. When we added Fe^{2+}, ALKBH2, the shear band was observed. However, when DFO was added into the repair system, a significant decrease of the shear DNA was found, indicating that DFO could influence the repair capability of ALKBH2 by depleting Fe^{2+}.

3.3. In vitro enhanced PDT of MFLs@5-ALA/DFO

The accumulation of PS (PpIX) in tumor cells leads to the more ROS generation during laser irradiation. Thereby, the levels of ROS in

B16−F10 cells after laser irradiation was further detected. As can be seen from Fig. 3A, only a low level of ROS was detected in the case of 5-ALA group, while the ROS significantly increased when combined with DFO, and the MFLs@5-ALA/DFO generated more ROS than that of other treatments. As mentioned above, the accumulation of PpIX results in generating more ROS in tumor cells, and the more ROS would lead to the more serious damage to cell contents. ROS usually causes the oxidative damage to DNA, therefore, γH2AX, which could form foci at the location of DNA damage, was chosen as a marker, and the DNA damage was explored by the amount of γH2AX (Fig. 3B). Relative gray value of γH2AX in 5-ALA + DFO group was higher than that in 5-ALA group, which might be ascribed to the down-regulation of Fe^{2+}, thus reduces the activity of DNA repair enzyme and promotes the accumulation of PpIX. As expected, MFLs@5-ALA/DFO induced most DNA damage with the synergic enhanced drug delivery of MFLs. The DNA damage was also evaluated by comet assays. As shown in Fig. 3C, the tail DNA percentage of 10.9% in MFLs@5-ALA/DFO group was significantly higher than that in other groups (0.2% in control group, 1.7% in 5-ALA group, 2.3% in DFO group and 7.8% in 5-ALA + DFO group), consistent with the γH2AX assays. The activity of DNA repair enzymes plays an important role in maintaining homologous recombination of DNA. Therefore, the reduction of the activity of DNA repair enzymes will lead to a visible damage in DNA. Therefore, in the case of DFO group, an obvious DNA damage was also observed (Fig. 3B and C). Next, the cell viability of B16−F10 tumor cells receiving different treatments (with 532 nm laser) were further investigated. As shown in Fig. 3D, when the concentration of 5-ALA was 2 mmol/L, the cell viability of 5-ALA was 49.0%, while a significant decreasing in the cell viability (30.0%) was observed in the case of 5-ALA + DFO group. In the case of MFLs@5-ALA/DFO group, after treatment, the cell viability decreased to 20.0%, much lower than that of 5-ALA or 5-ALA + DFO group, indicating that MFLs@5-ALA/DFO could boost the PDT of 5-ALA through intracellular iron regulating strategy. At the same time, we also detected the cell viability of DFO. It can be seen from Supporting Information Fig. S11 that when the concentration of DFO reaches 400 μmol/L, the cell viability reaches 50.0%. The enhanced PDT of MFLs@5-ALA/DFO was further investigated by a live/dead cell staining assay, green fluorescence represents living cells and red fluorescence represents dead cells (Fig. 3E). As expected, more dead cells were found in MFLs@5-ALA/DFO group, which is consistent with the above results. Finally, apoptosis of B16−F10 tumor cells receiving different treatments were detected, and the results are shown in Fig. 3F. The apoptosis rate of 39.3% in MFLs@5-ALA/DFO group was significantly higher than that in other groups (5.5% in control group, 10.1% in 5-ALA group, 11.2% in DFO group and 26.0% in 5-ALA + DFO group), further confirmed the enhanced PDT of MFLs@5-ALA/DFO.

3.4. In vivo enhanced PDT of MFLs@5-ALA/DFO

IR780, a near-infrared dye, was used to indicate MFLs and CLs, respectively. As shown in Fig. 4A, the fluorescence signal at the tumor site of MFLs@IR780 and CLs@IR780 group increased steadily over time. Interestingly, the fluorescence in tumor site was still relatively high even at 36 h post-injection. Furthermore, MFLs@IR780 was accumulated in the tumor region efficiently compared to CLs@IR780 even at 36 h post-injection, demonstrating that MFLs also had a better tumor-targeting ability than CLs. This dramatic difference might be ascribed to the enhanced blood circulation stability and passive targeting of MFLs@IR780
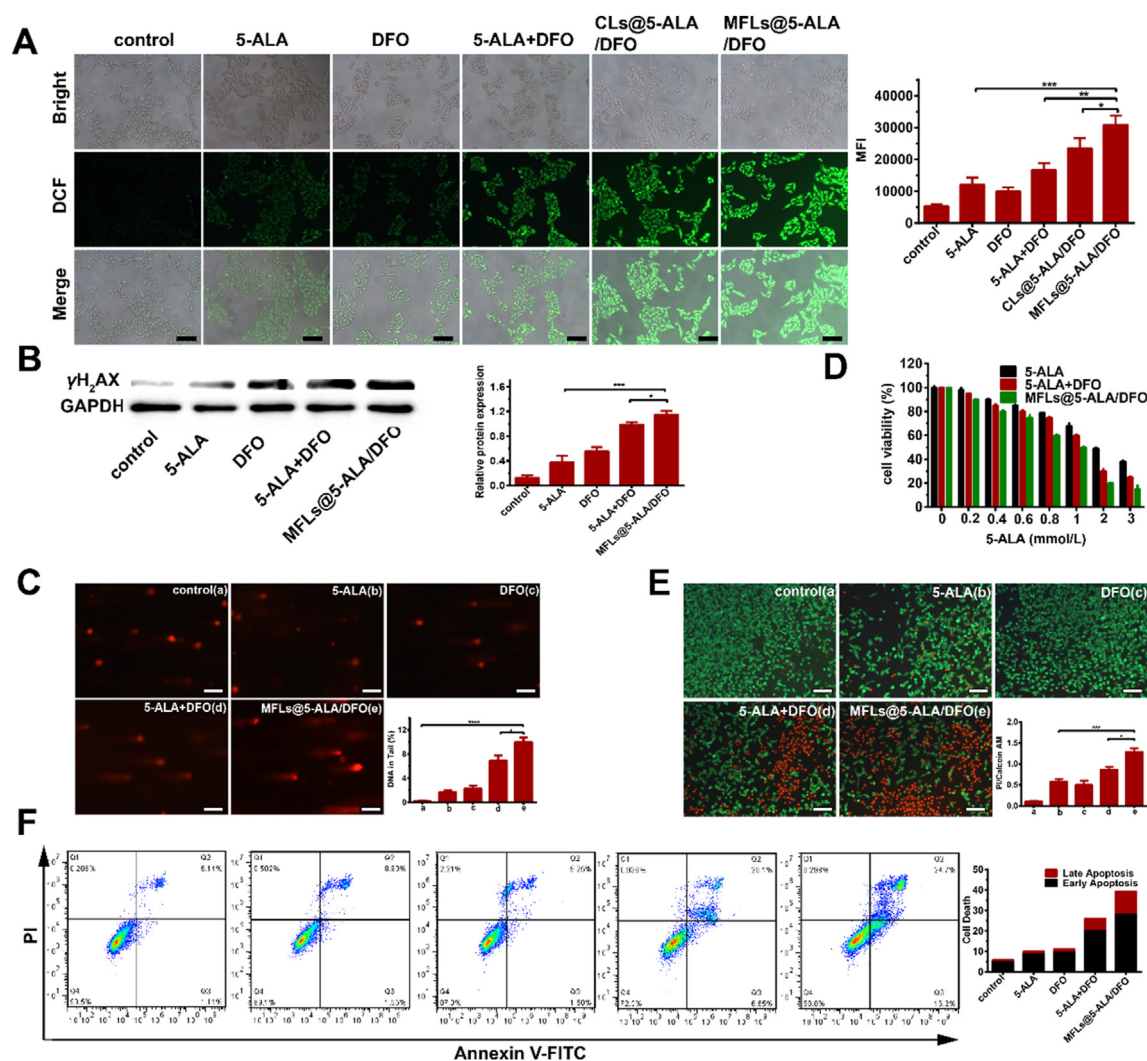
Figure 3 *In vitro* enhanced PDT of MFLs@5-ALA/DFO. (A) The production of reactive oxygen species (ROS) after 532 nm laser irradiation by fluorescence microscope (scale bar = 200 μm). (B, C) The analyzed of DNA damage by western blotting and comet assay (scale bar = 200 μm). (D) Cells cytotoxicity of 5-ALA, 5-ALA + DFO, MFLs@5-ALA/DFO. (E) Living and dead cell staining and apoptosis test by Calcein-AM and Propidium Iodide (Calcein-AM/PI) (scale bar = 200 μm). (F) Annexin V/PI staining assays of B16−F10 cells. All of them were incubated with different preparations for 4 h and irradiated with 532 nm laser. Data are presented as means ± SD (n = 3). ***P < 0.001, **P < 0.01, *P < 0.05.

endowed by the liposomes coating and nanoscale size, while free IR780 is rapidly excreted from body because of its instability.

The encouraging results *in vitro* and excellent tumor accumulation ability of MFLs@5-ALA/DFO inspire us further investigated the antitumor effect *in vivo*. B16−F10 tumor-bearing C57 mice were randomly divided into seven groups (n = 6) and then intravenous injection with different formulations, respectively. As shown in Fig. 4B, progressive growth of tumor were observed in saline, 5-ALA, DFO, 5-ALA + DFO and MFLs@5-ALA-treated groups. However, tumor growth inhibition in varying degrees were observed in mice after treatment with CLs@5-ALA/DFO and MFLs@5-ALA/DFO. As expected, in the presence of laser irradiation, the tumor growth in MFLs@5-ALA/DFO group was maximally inhibited than that of other groups, which was ascribed to excellent tumor accumulation and DFO-mediated enhanced PDT. In addition, the tumor picture and tumor weight in mice after receiving different treatments displayed a similar trend (Fig. 4C and D). We also monitored the weight of 14 days tumor bearing

mice. As shown in Supporting Information Fig. S12, the weight of mice in each group gained weight. This also shows that different preparations have no obvious toxic and side effects on mice.

In addition, to study the therapeutic mechanism, Fe^{2+} and ROS in tumor tissues were detected, respectively. As shown in Fig. 4E and Supporting Information Fig. S13, compared with the saline-treated group, the fluorescence intensity (Fe^{2+}) in the CLs@5-ALA/DFO and MFLs@5-ALA/DFO groups were significantly weakened. Particularly, the MFLs@5-ALA/DFO group showed the lowest fluorescence intensity (Fe^{2+}) compared with other groups. The reason is that the MFLs can efficiently deliver DFO to the tumor and quickly delete Fe^{2+}. Next, the intra-tumoral distribution of MFLs was performed by using the fluorescence of PpIX in tumor tissues. After the B16−F10 tumor-bearing mice receiving different treatments, the PpIX in tumor tissues were also investigated (Fig. 4F and Supporting Information Fig. S14). According to the results, a significant increase of red fluorescence (PpIX) was observed in 5-ALA,
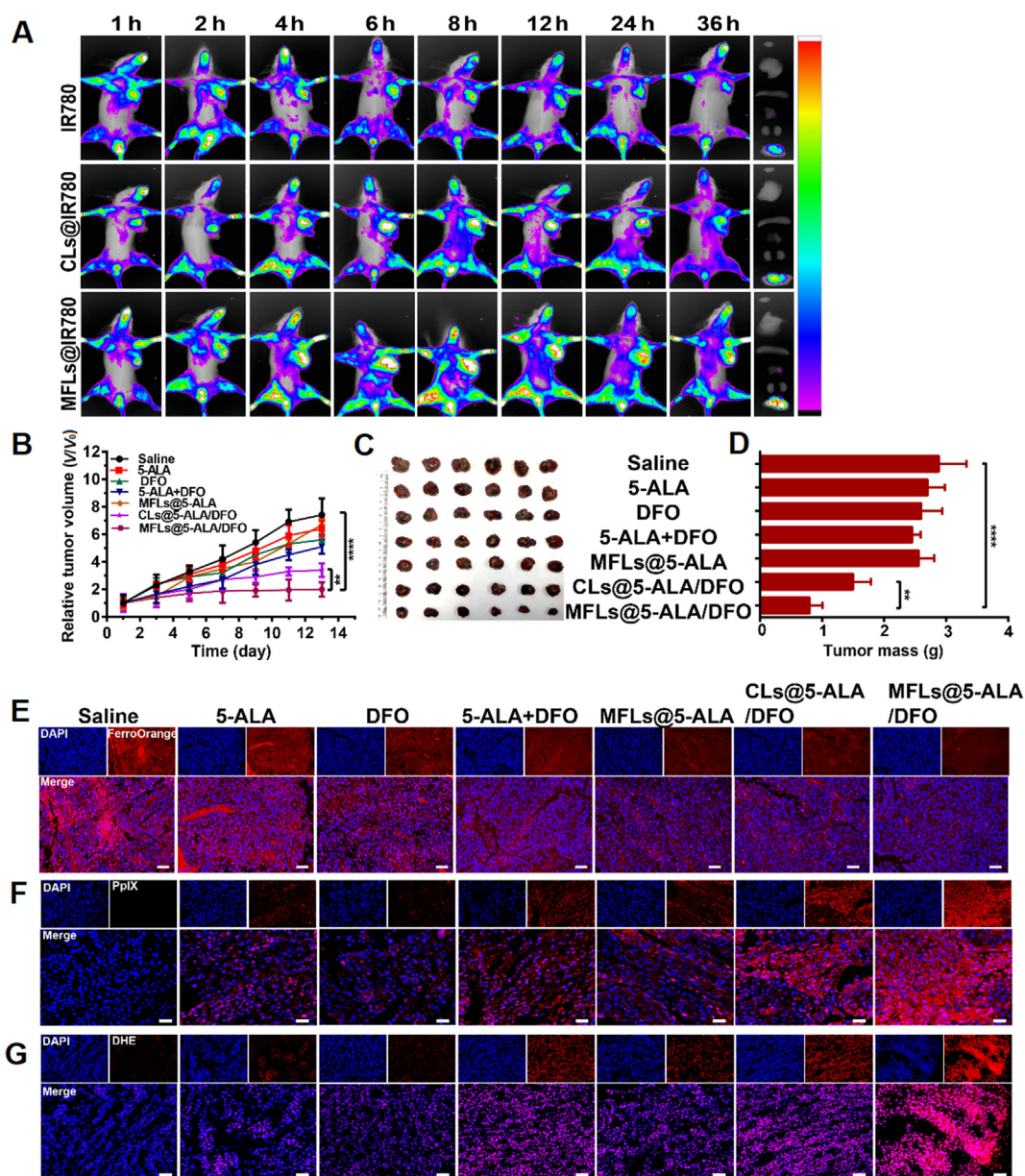
Figure 4 The NIR fluorescence imaging and antitumor efficacy *in vivo*. (A) *In vivo* fluorescence images of tumor-bearing mice at different time points after intravenous injection of IR780, CLs@IR780 and MFLs@IR780. (B) The relative tumor volume (C) the images of the tumor-bearing mice (D) tumor mass after treated 14 days with different preparations ($n = 6$). The detection of Fe^{2+} (E), ROS (F) and PpIX (G) in tumor tissues. The tumor tissues were exfoliated from different groups after treated 14 days with different preparations. Scale bar $= 50$ μm. Data are presented as means $\pm$ SD ($n = 3$). ****$P < 0.0001$, **$P < 0.01$.

DFO, 5-ALA + DFO, MFLs@5-ALA, CLs@5-ALA/DFO and MFLs@5-ALA/DFO groups. However, compared with 5-ALA group, 5-ALA + DFO displayed a higher level of PpIX, indicating that the reduction of the intracellular iron realizes a significant increase of intracellular accumulation of PpIX. Furthermore, more PpIX fluorescence was observed in MFLs@5-ALA/DFO group than that in CLs@5-ALA/DFO (with the same concentration of 5-ALA and DFO), once again proved that MFLs had more advantages than CLs. In addition, the amount of ROS production was the highest in MFLs@5-

ALA/DFO group compared to other groups, confirming that the nanosystem-mediated rapid iron deletion increased the intracellular accumulation of PpIX, thereby increasing the production of ROS (Fig. 4G and Supporting Information Fig. S15).

Then tumor slices were stained with TUNEL and H&E. As shown in Supporting Information Fig. S16, compared with saline group, no significant histological differences were observed in 5-ALA, DFO, 5-ALA + DFO and MFLs@5-ALA groups. However, a large number of apoptosis characteristics (nuclei contract, decompose) were found in the CLs@5-ALA/

DFO and MFLs@5-ALA/DFO-treated groups, especially in MFLs@5-ALA/DFO group. Furthermore, the results of TUNEL staining show a similar trend, further proved its excellent ability to induce apoptosis. Moreover, the body weight change curves of the mice during treatment in each group were similar. Also, H&E images of major organs (lung, liver, spleen, kidney, and heart) exhibited no noticeable pathological abnormalities in MFLs@5-ALA/DFO group (Supporting Information Fig. S17), demonstrating its systemic compatibility and tissue safety, which post a potential for further biomedicine application.

4. Conclusions

In summary, we have successfully synthesized a liposomal nanomedicine (MFLs@5-ALA/DFO) with intracellular iron regulation and improved pharmaceutical behavior, as well as the tumor cell membrane fusion properties for boosting the PDT of 5-ALA. The prepared MFLs@5-ALA/DFO presents a robust PDT in tumor cell: i) efficiently reduce the intracellular iron ion, thus blocking the biotransformation of photosensitive PpIX to HEME, realizing a significant increase of intracellular PpIX; ii) inhibit the activity of DNA repair enzyme in tumor cells with the decrease of the intracellular iron ion, achieving the aggravated DNA damage induced by the generated ROS during PDT. Such a liposomal nanomedicine that integrating the interference of natural 5-ALA biotransformation and the reversal of damaged DNA repair through iron ion regulation significantly enhance the PDT efficiency of 5-ALA.

Author contributions

Jinjin Shi, Junjie Liu, Kaixiang Zhang and Wei Liu designed the research. Airong Li and Chenglin Liang carried out the experiments and performed data analysis. Lihua Xu, Yiyang Wang participated part of the experiments. Jinjin Shi, Junjie Liu, Kaixiang Zhang provided experimental drugs and quality control. Jinjin Shi and Chenglin Liang wrote the manuscript. Jinjin Shi revised the manuscript. All of the authors have read and approved the final manuscript.

Conflicts of interest

The authors have no conflicts of interest to declare.

Appendix A. Supporting information

Supporting data to this article can be found online at https://doi.org/10.1016/j.apsb.2021.03.017.

References

1. Ma X, Qu QY, Zhao YL. Targeted delivery of 5-aminolevulinic acid by multifunctional hollow mesoporous silica nanoparticles for photodynamic skin cancer therapy. *ACS Appl Mater Interfaces* 2015;**7**:10671−6.
2. Wu JN, Han HJ, Jin Q, Li ZH, Li HA, Ji J. Design and proof of programmed 5-aminolevulinic acid prodrug nanocarriers for targeted photodynamic cancer therapy. *ACS Appl Mater Interfaces* 2017;**9**:14596−605.
3. Kwiatkowski S, Knap B, Przystupski D, Saczko J, Kedzierska E, Knap-Czop K, et al. Photodynamic therapy—mechanisms, photosensitizers and combinations. *Biomed Pharmacother* 2018;**106**:1098−107.
4. Abrahamse H, Hamblin MR. New photosensitizers for photodynamic therapy. *Biochem J* 2016;**473**:347−64.
5. Yan YW, Zhang KX, Wang HL, Liu W, Zhang ZZ, Liu JJ, et al. A fullerene based hybrid nanoparticle facilitates enhanced photodynamic therapy *via* changing light source and oxygen consumption. *Colloids Surf B Biointerfaces* 2020;**186**:110700.
6. Lucky SS, Soo KC, Zhang Y. Nanoparticles in photodynamic therapy. *Chem Rev* 2015;**115**:1990−2042.
7. Liu JJ, Zhang YW, Liu W, Zhang KK, Shi JJ, Zhang ZZ. Tumor antigen mediated conformational changes of nanoplatform for activated photodynamic therapy. *Adv Healthc Mater* 2019;**8**:e1900791.
8. Morales EH, Pinto CA, Luraschi R, Munoz-Villagran CM, Cornejo FA, Simpkins SW, et al. Accumulation of heme biosynthetic intermediates contributes to the antibacterial action of the metalloid tellurite. *Nat Commun* 2017;**8**:15320.
9. Piffaretti D, Burgio F, Thelen M, Kaelin-Lang A, Paganetti P, Reinert M, et al. Corrigendum to "Protoporphyrin IX tracer fluorescence modulation for improved brain tumor cell lines visualization. *J Photochem Photobiol B* 2020;**205**:111828.
10. Tewari KM, Eggleston IM. Chemical approaches for the enhancement of 5-aminolevulinic acid-based photodynamic therapy and photodiagnosis. *Photochem Photobiol Sci* 2018;**17**:1553−72.
11. Herceg V, Lange N, Allemann E, Babic A. Activity of phosphatase-sensitive 5-aminolevulinic acid prodrugs in cancer cell lines. *J Photochem Photobiol B* 2017;**171**:34−42.
12. Bragagni M, Scozzafava A, Mastrolorenzo A, Supuran CT, Mura P. Development and *ex vivo* evaluation of 5-aminolevulinic acid-loaded niosomal formulations for topical photodynamic therapy. *Int J Pharm* 2015;**494**:258−63.
13. Juzeniene A, Juzenas P, Moan J. Application of 5-aminolevulinic acid and its derivatives for photodynamic therapy *in vitro* and *in vivo*. *Methods Mol Biol* 2010;**635**:97−106.
14. Abo-Zeid MAM, Abo-Elfadl MT, Mostafa SM. Photodynamic therapy using 5-aminolevulinic acid triggered DNA damage of adenocarcinoma breast cancer and hepatocellular carcinoma cell lines. *Photodiagnosis Photodyn Ther* 2018;**21**:351−6.
15. Briel-Pump A, Beez T, Ebbert L, Remke M, Weinhold S, Sabel MC, et al. Accumulation of protoporphyrin IX in medulloblastoma cell lines and sensitivity to subsequent photodynamic treatment. *J Photochem Photobiol B* 2018;**189**:298−305.
16. Fontana AO, Piffaretti D, Marchi F, Burgio F, Faia-Torres AB, Paganetti P, et al. Epithelial growth factor receptor expression

influences 5-ALA induced glioblastoma fluorescence. *J Neuro Oncol* 2017;**133**:497−507.

17. Ohgari Y, Nakayasu Y, Kitajima S, Sawamoto M, Mori H, Shimokawa O, et al. Mechanisms involved in delta-aminolevulinic acid (ALA)-induced photosensitivity of tumor cells: relation of ferrochelatase and uptake of ALA to the accumulation of protoporphyrin. *Biochem Pharmacol* 2005;**71**:42−9.

18. Lu NH, Yi L, Deng QQ, Li JY, Gao ZH, Li HL. The interaction between desferrioxamine and hemin: a potential toxicological implication. *Toxicol Vitro* 2012;**26**:732−5.

19. Wang LJ, Li XQ, Mu YX, Lu C, Tang SQ, Lu K, et al. The iron chelator desferrioxamine synergizes with chemotherapy for cancer treatment. *J Trace Elem Med Biol* 2019;**56**:131−8.

20. Wang WQ, Tabu KC, Hagiya Y, Sugiyama Y, Kokubu Y, Murota Y, et al. Enhancement of 5-aminolevulinic acid-based fluorescence detection of side population-defined glioma stem cells by iron chelation. *Sci Rep* 2017;**7**:42070.

21. Döring F, Walter J, Will J, Föcking M, Boll M, Amasheh S, et al. Delta-aminolevulinic acid transport by intestinal and renal peptide transporters and its physiological and clinical implications. *J Clin Invest* 1998;**101**:2761−7.

22. Puente BN, Kimura W, Muralidhar SA, Moon J, Amatruda JF, Phelps KL, et al. The oxygen-rich postnatal environment induces cardiomyocyte cell-cycle arrest through DNA damage response. *Cell* 2014;**157**:565−79.

23. Weeden CE, Asselin-Labat ML. Mechanisms of DNA damage repair in adult stem cells and implications for cancer formation. *Biochim Biophys Acta Mol Basis Dis* 2018;**1864**:89−101.

24. Li Q, Huang Y, Liu XC, Gan JH, Chen H, Yang CG. Rhein inhibits AlkB repair enzymes and sensitizes cells to methylated DNA damage. *J Biol Chem* 2016;**291**:11083−93.

25. Chen FY, Tang Q, Ma H, Bian K, Seeram NP, Li DY. Hydrolyzable tannins are iron chelators that inhibit DNA repair enzyme ALKBH2. *Chem Res Toxicol* 2019;**32**:1082−6.

26. Tarafdar PK, Chakraborty H, Dennison SM, Lentz BR. Phosphatidylserine inhibits and calcium promotes model membrane fusion. *Biophys J* 2012;**103**:1880−9.

27. Haque ME, Mclntosh TJ, Lentz BR. Influence of lipid composition on physical properties and PEG-mediated fusion of curved and uncurved model membrane vesicles: "Nature's own" fusogenic. *Biochemistry* 2001;**40**:4340−8.

28. Yang J, Bahreman A, Daudey G, Bussmann J, Olsthoorn RCL, Kros A. Drug delivery *via* cell membrane fusion using lipopeptide modified liposomes. *ACS Cent Sci* 2016;**2**:621−30.

29. Stender IM, Na R, Fogh H, Gluud C, Wulf HC. Photodynamic therapy with 5-aminolaevulinic acid or placebo for recalcitrant foot and hand warts: randomised double-blind trial. *Lancet* 2000;**355**:963−6.

30. Wang BH, Zhang HF, An JY, Zhang YW, Sun LL, Jin YJ, et al. Sequential intercellular delivery nanosystem for enhancing ROS-induced antitumor therapy. *Nano Lett* 2019;**19**:3505−18.

31. Lin MW, Huang YB, Chen CL, Wu PC, Chou CY, Wu PC, et al. A formulation study of 5-aminolevulinic encapsulated in DPPC liposomes in melanoma treatment. *Int J Med Sci* 2016;**13**:483−9.

32. Tran TQ, Ishak Gabra MB, Lowman XH, Yang Y, Reid MA, et al. Glutamine deficiency induces DNA alkylation damage and sensitizes cancer cells to alkylating agents through inhibition of ALKBH enzymes. *PLoS Biol* 2017;**15**:e2002810.

33. Liu W, Zhang KX, Zhuang LY, Liu JJ, Zeng W, Shi JJ, et al. Aptamer/photosensitizer hybridized mesoporous MnO$_2$ based tumor cell activated ROS regulator for precise photodynamic therapy of breast cancer. *Colloids Surf B Biointerfaces* 2019;**184**:110536.

34. Shi JJ, Yu WY, Xu LH, Yin N, Liu W, Zhang KX, et al. Bioinspired nanosponge for salvaging ischemic stroke *via* free radical scavenging and self-adapted oxygen regulating. *Nano Lett* 2020;**20**:780−9.

35. Wang W, Luo SM, Ma JY, Shen W, Yin S. Cytotoxicity and DNA damage caused from diazinon exposure by inhibiting the PI3K-AKT pathway in porcine ovarian granulosa cells. *J Agric Food Chem* 2019;**67**:19−31.

36. Prasad RY, Wallace K, Daniel KM, Tennant AH, Zucker RM, Jenna Strickland J, et al. Effect of treatment media on the agglomeration of titanium dioxide nanoparticles: impact on genotoxicity, cellular interaction, and cell cycle. *ACS Nano* 2013;**7**:1929−42.

37. Torti SV, Manz DH, Paul BT, Blanchette-Farra N, Torti FM. Iron and cancer. *Annu Rev Nutr* 2018;**38**:97−125.

38. Thévenod F. Iron and its role in cancer defense: a double-edged sword. *Met Ions Life Sci* 2018;**18**:437−67.